NANO LETTERS

pubs.acs.org/NanoLett Letter

Dual Control of Enhanced Quasi-Bound States in the Continuum Emission from Resonant c-Si Metasurfaces

Zhenghe Zhang,[⊥] Chaojie Xu,[⊥] Chen Liu, Man Lang, Yuehao Zhang, Minghao Li, Wanli Lu, Zefeng Chen, Chinhua Wang, Shaojun Wang,* and Xiaofeng Li*

Cite This: *Nano Lett.* 2023, 23, 7584−7592 Read Online

ACCESS | Metrics & More | Article Recommendations | Supporting Information

ABSTRACT: Optical bound states in the continuum (BICs) offer strong interactions with quantum emitters and have been extensively studied for manipulating spontaneous emission, lasing, and polariton Bose−Einstein condensation. However, the out-coupling efficiency of quasi-BIC emission, crucial for practical light-emitting devices, has received less attention. Here, we report an adaptable approach for enhancing quasi-BIC emission from a resonant monocrystalline silicon (c-Si) metasurface through lattice and multipolar engineering. We identify dual-BICs originating from electric quadrupoles (EQ) and out-of-plane magnetic dipoles, with EQ quasi-BICs exhibiting concentrated near-fields near the c-Si nanodisks. The enhanced fractional radiative local density of states of EQ quasi-BICs overlaps spatially with the emitters, promoting efficient out-coupling. Furthermore, coupling the EQ quasi-BICs with Rayleigh anomalies enhances directional emission intensity, and we observe inherent opposite topological charges in the multipolarly controlled dual-BICs. These findings provide valuable insights for developing efficient nanophotonic devices based on quasi-BICs.

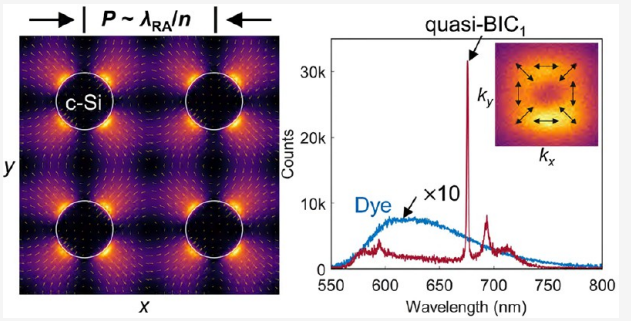

KEYWORDS: *radiation efficiency, optical bound states in the continuum, dielectric nanoantenna array, multipolar control, collective resonances, polarization-vortex emission*

Optical bound states in the continuum (BICs) have become crucial for designing optoelectronic devices in the past decade.[1−11] BICs are a type of resonances that can be confined within the radiation continuum using periodic photonic structures like photonic crystals, metasurfaces, gratings, and waveguides.[2,12−17] Through destructive interference or symmetry protection, BICs prevent resonance from radiating into free space, offering infinite quality (Q) factor and topological protection via polarization singularity.[12,13,15,18] Operating in the "quasi-BIC" zone, devices can achieve high Q-factors, enabling strong interactions with quantum emitters such as dye molecules and quantum dots within their leakage channel.[19]

Recent research has extensively explored the utilization of quasi-BICs for manipulating spontaneous emission and lasing.[20−24] These quasi-BICs, arising from coherent oscillations of electric and magnetic multipoles within periodic photonic systems, have enabled low-threshold lasing with multiple topological vortex options and a wide range of wavelengths.[25−27] Strong coupling with excitons has even facilitated polariton Bose−Einstein condensation.[6] Structural symmetry breaking has been employed to split the topological charge carried by BIC into two halves, resulting in high-purity and directionally chiral light emission.[7,9] These advancements have significantly enhanced our understanding of manipulating topological and chiral emission as well as reducing lasing thresholds, driven by the infinite Q-factors of BICs. However, the practical implementation of light-emitting devices, like light-emitting diodes and lasers, requires careful consideration of the out-coupling efficiency, which determines how efficiently generated light is extracted and emitted into free space in the desired direction. To the best of our knowledge, there is a noticeable lack of research focused on enhancing the out-coupling efficiency of quasi-BIC emission.

Here, we demonstrate simultaneous control over quasi-BIC emission from a resonant monocrystalline silicon (c-Si) metasurface through lattice and multipolar engineering. By analyzing wave-vector resolved extinction spectra and near-field properties, we identify the presence of dual-BICs originating from electric quadrupoles (EQ) and out-of-plane magnetic dipoles (MD_z). The near-fields for EQ quasi-BICs are concentrated in the proximity of the c-Si nanodisks, resulting in an elevated fractional optical local density of states

Received: June 9, 2023
Revised: July 26, 2023
Published: August 4, 2023

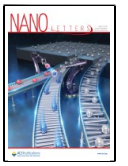

https://doi.org/10.1021/acs.nanolett.3c02148
Nano Lett. 2023, 23, 7584−7592

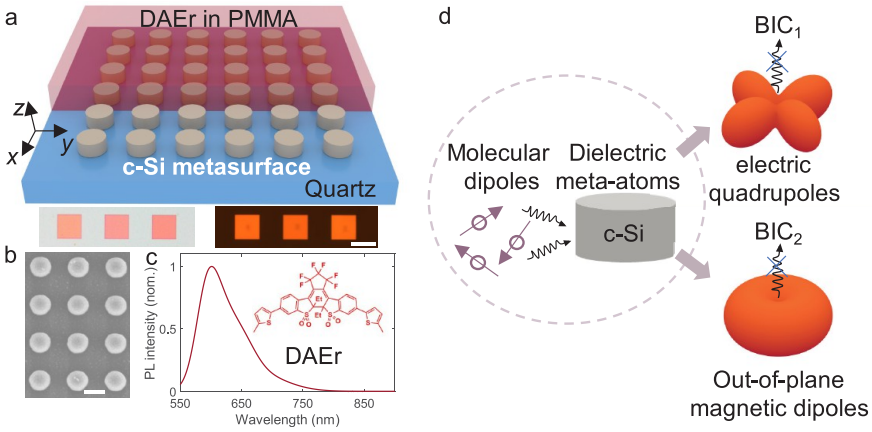

Figure 1. Resonant c-Si metasurfaces. (a) Schematic of the sample. (Bottom) The left panel is the bright-field microscope image of three array samples and the right one is their photoluminescence (PL) image. (b) Top-view SEM image of the sample. (c) PL spectrum of the dye molecules (DAEr) doped in PMMA. Inset shows the molecular structure of DAEr. (d) Spontaneous emission of molecular dipoles drives the collective Mie-resonances of the nanodisks in terms of the near-field coupling. The multipoles inside the nanodisks re-emit the light to the free space. Due to the symmetry protection in electric/magnetic quadrupoles (EQ/MQ) or out-of-plane electric/magnetic dipoles (ED_z/MD_z), their radiation channel normal to the metasurface is fully suppressed, leading to the bound states in the continuum (BICs). Scale bars: (a) 50 μm and (b) 200 nm.

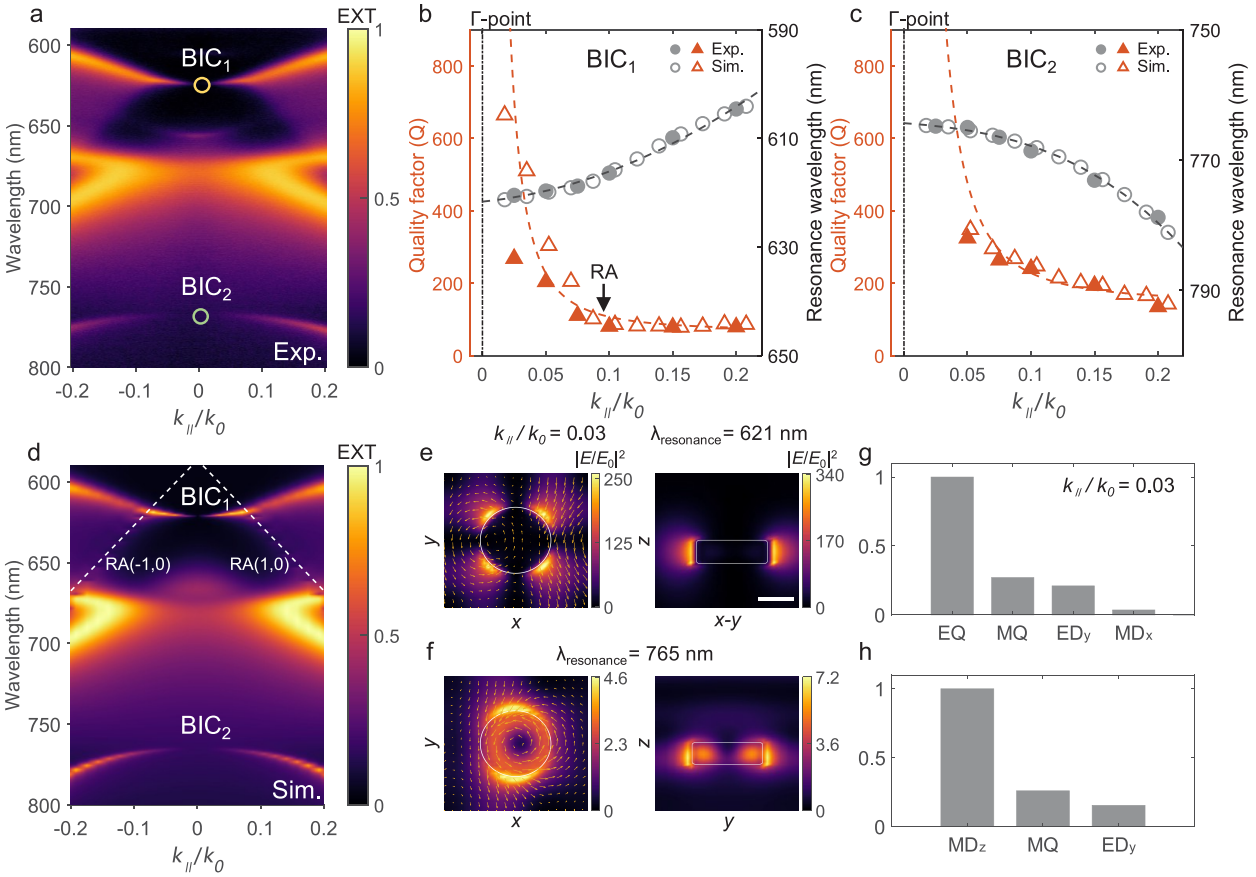

Figure 2. Verification of dual symmetry-protected BICs. (a,d) The wave-vector resolved extinction spectra measured and simulated with TE-polarized light. The periodicity of the array sample herein is 405 nm. The circles at the Γ-point represent the resonances for two BICs in panel a. The white-dashed lines represent the angular dispersion for the resonances of RA in panel d. (b,c) Analysis of the quality factors (orange triangles) and resonance wavelength (gray circles) as a function of the incident wave-vectors around BIC_1 and BIC_2 resonances. The fitted curves are shown with different colors. The black vertical line indicates the Γ-point. (e,f) Top view and side view of the field intensity enhancement in a unit cell. The calculated resonances are close to the BICs, namely, quasi-BICs. The yellow arrows on the top-view distribution represent the real components of the electric vector field projected in the *xy*-planes. Scale bar: 100 nm. (g,h) The corresponding weights of the multipolar composition for the two resonances shown in panels e and f.

(LDOS) for emitters. By differentiating the wavelengths between Rayleigh anomaly (RA) resonances and quasi-BICs, we observe directional emission from quasi-BICs with a defined wave-vector, achieving an ~90-fold photoluminescence

https://doi.org/10.1021/acs.nanolett.3c02148
Nano Lett. 2023, 23, 7584−7592

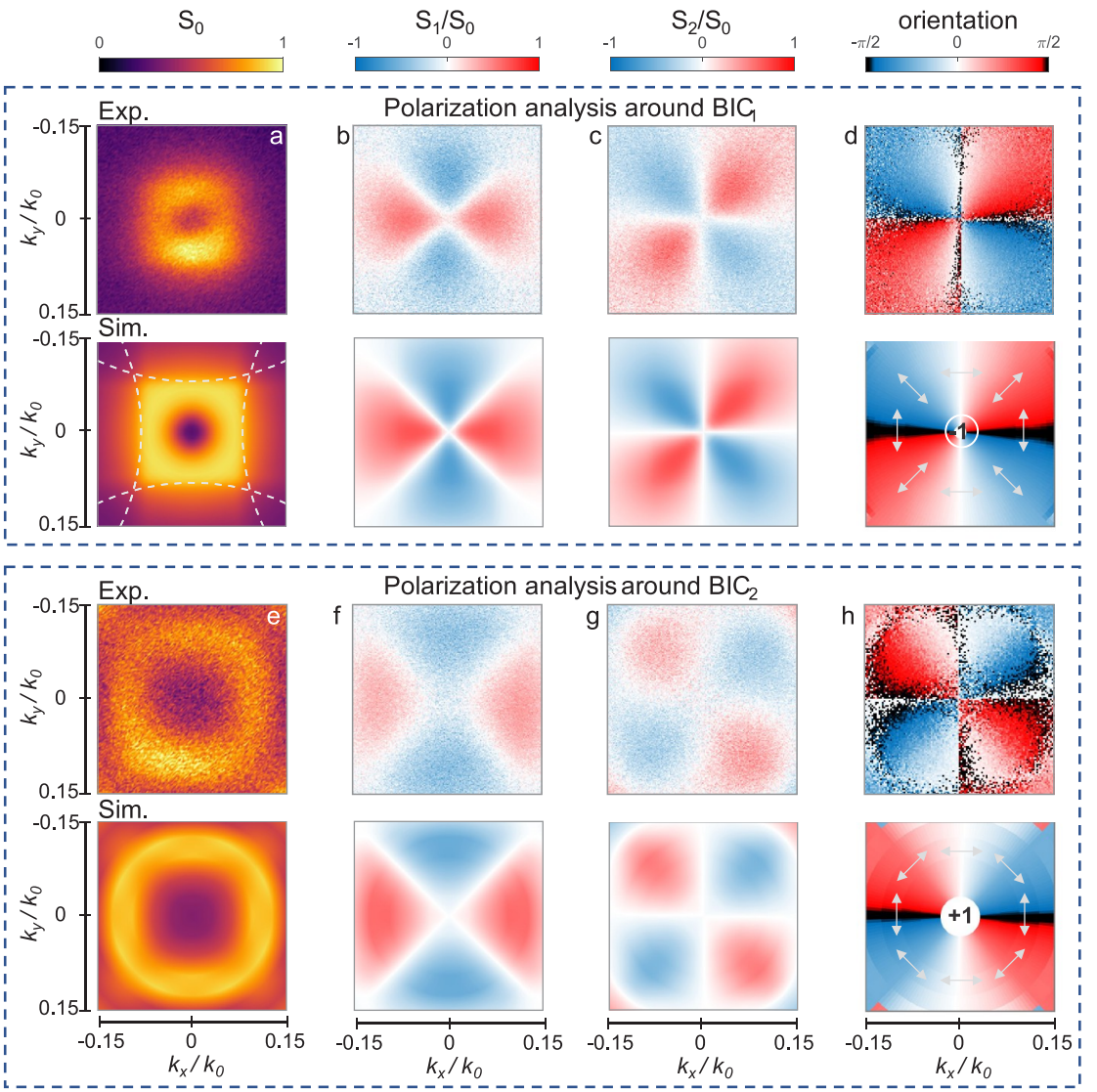

Figure 3. (Top) Multipolar control of polarization-vortex emission. Stokes parameters S_0 (a,e), S_1 (b,f), S_2 (c,g), and the polarization angle (d,h) for the emission signals around BIC_1 and BIC_2, which are measured in the wave-vector space. (Bottom) Corresponding simulation results based on reciprocity. The polarization singularity for two BICs are characterized by the topological charge of $q = -1$ and $+1$, respectively.

enhancement (PLE) at 680 nm, which is significantly more efficient than previous studies involving plasmonic and Mie surface lattice resonances (SLRs),[28−31] as well as the recently reported quasi-BICs in photonic crystals.[23,24] Using an accurate Stokes parameters method, we also observe inherent opposite topological charges in the multipolar controlled dual-BICs. These findings offer insights for developing efficient, sensitive, and multifunctional nanophotonic devices.

First, we successfully fabricated a metasurface with c-Si, featured with low loss and high refractive indices in the visible light range.[32−35] The metasurface is transferred onto a quartz substrate using a "floating off" technique and fixed on quartz by dangling bonding at the interface between c-Si and quartz, and a 300-nm-thick PMMA polymer doped with 0.1 wt % high-quantum-yield dye molecules [diarylethene red (DAEr)] is spin-coated onto the surface (Figure S1).[36] The bright-field and fluorescence microscopy images of three array samples are shown at the bottom of Figure 1a. Uniform diameters of the nanodisks (D = 200 nm) and periodicity of the array (P = 405 nm) are confirmed with SEM (Figure 1b), and the normalized PL spectrum and compound structure of DAEr are also illustrated in Figure 1c. The DAEr emits light at a central wavelength of 600 nm with a line width of 80 nm, which coincides with the resonances of quasi-BICs that will be discussed further below. We exploit the strong near-field confinement properties of BICs to enhance fluorescence. By arranging the periodicity of a square lattice below the first orders of RA, we create favorable conditions for collective Mie resonances within the array plane. This promotes strong light−matter interactions in the emitting layer covering the c-Si metasurface. Upon excitation, DAErs act as point dipoles, triggering near-field electromagnetic resonances (EQ and MD_z modes) in the c-Si nanoparticle meta-atoms. These meta-atoms form a C_2 symmetric square lattice, lacking any radiation channel in the normal direction.[37] Consequently, two symmetry-protected BICs (BIC_1 and BIC_2) emerge (Figure 1d).

To identify the symmetry-protected BICs located at the Γ-point, we utilized back-focal-plane imaging to measure the wave-vector resolved extinction spectra of the samples. The

https://doi.org/10.1021/acs.nanolett.3c02148
Nano Lett. 2023, 23, 7584−7592

spectra (Figure 2a) revealed the presence of two "dark modes" characterized by zero extinction at $k_{\parallel}/k_0 = 0$ (Γ-point), while gradually increasing in extinction away from the center while still maintaining some scattering capacity. The regions corresponding to these "dark modes" are highlighted with yellow and green circles, respectively. We performed FDTD simulations to reproduce the extinction spectra (Figure 2d). The RA (±1, 0), responsible for the periodic lattice resonance, was calculated using the first-order grating equation and is represented by linear white-dashed curves in Figure 2d. Interestingly, in the short-wavelength region (600−650 nm), the extinction bands below the RA curves exhibit a narrower and cleaner profile, whereas above the RA curves, the bands extend across a continuum and a broad spectral background (Figure 2a and d).

To investigate the "dark modes" in detail, we calculated the extinction spectra across a range of wave-vectors from $k_{\parallel}/k_0$ = 0 to 0.2. The resonance wavelengths and *Q*-factors of the two dark modes are then determined as a function of incident wavevectors (Figure 2b and c). For the short-wavelength dark mode, the *Q*-factor remains constant as the wave-vector decreases until it reaches 0.095, corresponding to the RA(1, 0) order. At this point, the influence of the radiation channel induced by the RA leads to a significant increase in the *Q*-factor residing within a clean background of zero extinction. The data fitted with $Q \propto 1/\theta^2$ (orange-dashed curves) indicate that the *Q*-factor approaches infinity as the incident wave-vector approaches the Γ-point, where radiation losses are fully suppressed. The "dark mode" at longer wavelengths follows a similar trend but exhibits a more rapid increase in the *Q*-factor as the wave-vector decreases. Based on the pronounced divergence of the *Q*-factors near the Γ-point, we primarily deduce that both dark modes correspond to symmetry-protected BICs, labeled BIC_1 and BIC_2 (Figure 2a and d). BIC_1 is influenced by the RA and exhibits distinct characteristics compared to BIC_2, including significant variations in the *Q*-factors and resides within a distinct region of zero extinction.

To gain a deeper understanding of the mode characteristics, we conducted simulations to analyze the electric field intensity profiles of the two quasi-BICs located at the dye layer position. The field intensity enhancement, relative to the incident plane waves, is represented in color as a function of spatial coordinates on the midheight (*xy*-plane) and cross-section (*yz*-plane) of the nanoparticles. The yellow arrows indicate the real components of the electric vector field in the *xy*-plane. Although the incident plane wave has $k_{\parallel}/k_0 = 0.03$, the resonance wavelength differs. A nonzero value of $k_{\parallel}/k_0$ is chosen to ensure the non-negligible extinction of the dual quasi-BICs. The simulation results reveal that the quasi-BIC_1 mode at 621 nm exhibits an EQ pattern in the *xy*-plane with four lobes in the diagonal directions of the nanodisk (Figure 2e). Additionally, the pattern suggests that the strong electric field enhancements are located outside the nanoparticle, but with subwavelength confinement out of the plane. In contrast, the quasi-BIC_2 mode at 765 nm displays a loop electric field inside the nanodisk in the *xy*-plane, corresponding to a MD_z resonance (Figure 2f). The *yz*-plane exhibits a spatial distribution of the electric field both inside and at the edges of the nanodisk. Importantly, the stronger electric field distribution of the quasi-BIC_1 mode allows for the design of field overlap with an ensemble of emitters distributed in a spatially extended volume within the lattice plane. This prompts the question of why the field intensity enhancement of quasi-BIC_1 near the RA resonance is nearly 2 orders of magnitude higher than that of quasi-BIC_2.

Furthermore, we performed mode decomposition to calculate the individual contributions of multipole moments to the total scattering cross-section for both BIC modes (Figure S4). The results show that quasi-BIC_1 at $k_{\parallel}/k_0 = 0.03$ is predominantly composed of EQ, MQ, and ED_y, while BIC_2 is mainly derived from the contributions of MQ, ED_y, and MD_z. We extract the scattering cross-sectional spectra for each mode and calculate the relative weights of the multipole attributes (Figure 2g and h). The scattering contribution from EQ represents the highest proportion in quasi-BIC_1, earning it the designation of EQ-BIC. Conversely, quasi-BIC_2 predominantly originates from the scattering contribution of MD_z, and thus it can be referred to as MD_z-BIC. We further conducted precise measurements using the Stokes parameters method to analyze the polarization properties of the emitted light in the vicinity of the dual-BICs (see the details in S6 of SI). The two BICs in Figure 3a and e exhibit a "donut" PL intensity distribution with suppressed far-field radiation at the Γ-point. Quasi-BIC_1 shows a square-shaped far-field pattern surrounded by four RA band lobes (white-dashed curves). In Figure 3b,c,f,g, the two quasi-BICs exhibit consistent polarization in S_1/S_0, but opposite polarization in the diagonal directions in S_2/S_0, indicating different linear vortex features. The rotation of linearly polarized vortices is observed in Figure 3d and h (gray double arrows), displaying clear topological polarization characteristics of two BICs with opposite topological charges of −1 and +1, respectively.

Our investigation focuses on the influence of the multipolar characteristics of quasi-BICs on emission enhancement. In our experiment, we employed an extended source with a central wavelength of 450 nm to excite the sample. We recorded wave-vector resolved PL spectra in the Fourier space and evaluated the out-coupling efficiency improvement using the PLE by comparing the PL intensity from the array to that from the bare dye film (Figure S5). The dispersion pattern of PLE (Figure 4a and c) qualitatively matches that of the extinction, indicating that the emission of the molecules couples to the multipole resonances of the c-Si metasurface. The PLE spectrum lacks a continuum and broad background due to the different excitation conditions between extinction and PLE measurements. Extinction is governed by interference between incident and scattered fields, while PLE is influenced by local field enhancements at the emitter positions.[38] In addition, Figure 4a,c demonstrates a significant emission from quasi-BIC_1 as the normalized wave-vector deviates from 0 to 0.095. In contrast, quasi-BIC_2 exhibits a negligible PLE value due to its relatively low near-field enhancement near the c-Si nanoparticles (mentioned in Figure 2f). Note that the presence of an SLR between the two BICs, resulting from enhanced radiative coupling between the nanoparticles through RA. The PLE of the SLR is higher than that of BIC_2 but lower than that of BIC_1.

To ensure the reliability of the PL measurement, we performed simulations to calculate the average near-field enhancement in the PMMA region surrounding the c-Si nanodisks. These simulations provide information about the fractional radiative LDOS and are connected to the experiments through reciprocity theorem, where the emission direction of a local source is favored when the local field at the source's position is highest for a plane wave incidence from that direction.[30,39] The simulation results in Figure 4b closely

https://doi.org/10.1021/acs.nanolett.3c02148
Nano Lett. 2023, 23, 7584−7592

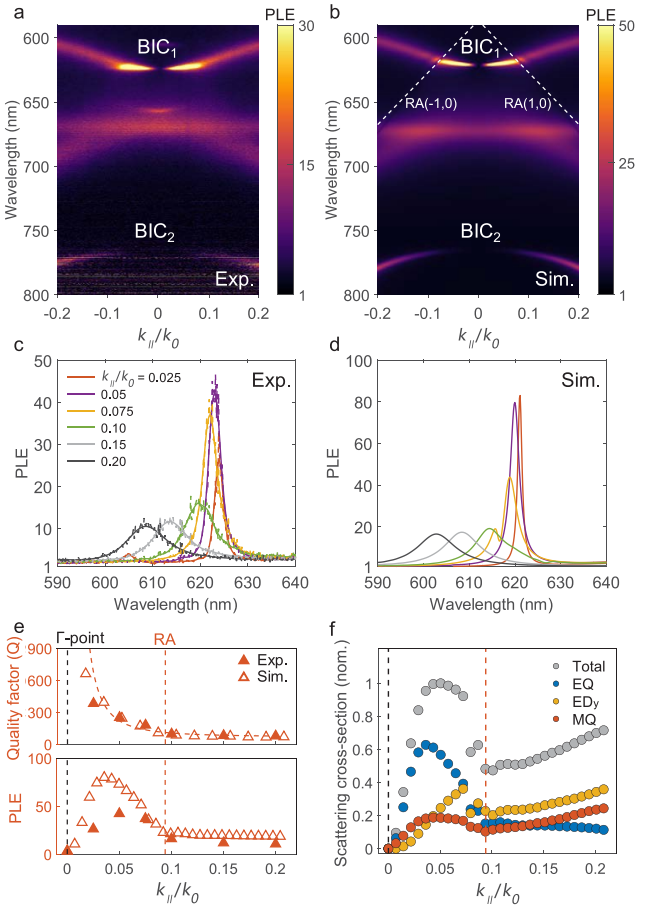

Figure 4. Multipolar control of enhanced light emission. (a,b) The wave-vector resolved emission enhancement corresponding to panels a and d in Figure 2. (c,d) The measured and simulated emission spectra for quasi-BIC_1 obtained by cutting through the dispersion curves in panels a and b. The experimental data points were fitted to a curve and displayed in various colors in panel c. (e,f) Analysis of the quality factors, photoluminescence enhancement (PLE), and the normalized scattering cross-section of the multipoles as a function of the incident wave-vectors around BIC_1 resonances. The total, EQ, MQ, and ED_y components are depicted as solid circles in different colors in panel f.

match the experimental data, although the simulated PLE values are higher than the measurements. Experimental limitations, such as imperfections in geometrical parameters and finite array size, may contribute to lower PLE factors in experiments compared to simulations.[40] The PLE of quasi-BIC_1 is affected by RA resonances, resulting in significant PLE differences inside and outside the RA band boundary.

Next, we extract the PLE spectra from the experimental and simulated results at different incident wave-vectors, focusing on quasi-BIC_1, as shown in Figure 4c and d. The experimental data (dotted-dashed lines) are well-fitted with the Lorentz function to mitigate the influence of spectral noise. The emission spectrum of the bare dye film is significantly tailored by coupling to the quasi-BIC resonances (Figures S5 and S8c). We calculate the *Q*-factors and PLE as a function of wave-vectors from the resonant peaks in Figure 4c,d and present them in Figure 4e. The trend of the *Q*-factor of BIC_1 with wave-vectors aligns closely with Figure 2b. PLE exhibits an increasing and then decreasing trend in the range of wave-vectors 0−0.095, reaching a maximum PLE around $k_{\parallel}/k_0$ = 0.03. Once the wave-vectors exceed the RA resonance (indicated by the vertical-dashed line in Figure 3e), the PLE tends to stabilize. To analyze the factors affecting PLE variation, we conducted calculations of normalized scattering cross-sections for total and multipolar contributions (EQ, ED_y, and MQ) with respect to incident wave-vectors, as shown in Figure 4f. Below the RA (±1, 0), EQ scattering contributes significantly and exhibits a trend comparable to that of the total scattering cross-section. As the wave-vector surpasses the RA resonance, the total scattering cross-section is predominantly influenced by ED_y and MQ resonances, which exhibit a gradual increase contrasting with the trend observed in PLE. It suggests that while quasi-BIC_1 is influenced by EQ, ED_y, and MQ scattering, the PLE is solely associated with EQ scattering.

By employing multipole decomposition, we have gained valuable insights into the significant role of the EQ resonance in the pronounced emission of quasi-BIC_1. However, the distinct variations in the PLE of quasi-BIC_1 above and below the RA band remain unexplained. To further investigate this phenomenon, we conducted experiments and simulations involving continuous tuning of *P* from 360 to 540 nm, while keeping *D* constant at 200 nm (Figure S6). Our results, presented in partial experimental and simulated data (Figure 5a−c and g−i), along with complete wave-vector resolved PL spectra (Figures S7 and S9), shed light on the relationship between *P* and PLE of quasi-BIC_1. They reveal that as *P* increases from 360 to 460 nm, the RA band gradually approaches quasi-BIC_1, resulting in a narrower range of wave-vectors within the RA bands for quasi-BIC_1 (Figure 5a−c and g−i). Despite this decrease, the maximum PLE of the sample continues to rise. However, once *P* exceeds 460 nm, the strongest PLE of quasi-BIC_1 starts to decline. At this point, the MD-SLR, which resembles a dispersion pattern of the RA (0, ±1) band below BIC_1,[35] gradually couples with quasi-BIC_1, leading to energy transfer between the quasi-BIC_1 resonance and MD-SLR. This ultimately results in high PLE of MD-SLR.

We further analyzed the wave-vector resolved PL spectra obtained from different periodicities, focusing on the spectra corresponding to the maximum PLE. The experimental and simulated spectra are shown in Figure 5d and j, respectively. We calculated the *Q*-factor, maximum PLE value, resonance wavelength of quasi-BIC_1, and wavelength difference ($\Delta\lambda$) relative to the RA resonance at the Γ-point for various periodicities, as summarized in Figure 5e,f,k,l, respectively. A positive correlation is observed between the *Q*-factor and the maximum PLE, indicating that quasi-BIC resonances with low losses are a necessary condition but not sufficient for achieving highly efficient out-coupling of emission. Both parameters initially increase and then decrease as the periodicity of the lattice increases. In the experimental data (Figure 5e and f), when *P* = 460 nm, with $\Delta\lambda$ = 9 nm, the line width of quasi-BIC_1 resonance is 1.1 nm, suggesting that the maximum *Q*-factor is ∼600, while the maximum PLE is ∼92 at *P* = 440 nm. Simulation results (Figure 5k and l) show a maximum *Q*-factor of 1000 at *P* = 480 nm with a corresponding maximum PLE of ∼180 at *P* = 460 nm. Note that the *Q*-factor and PLE do not reach their maximum values at the same periodicity, possibly due to the influence of the coupled MD-SLR. The resonance wavelength of the RA resonance at the Γ-point and the maximum PLE for quasi-BIC_1 gradually redshift as *P* increases, with the resonance redshift slope slightly larger than that of quasi-BIC_1. As a result, the wavelength difference ($\Delta\lambda$) between the two resonances (black squares in Figure 5f and

https://doi.org/10.1021/acs.nanolett.3c02148
Nano Lett. 2023, 23, 7584−7592

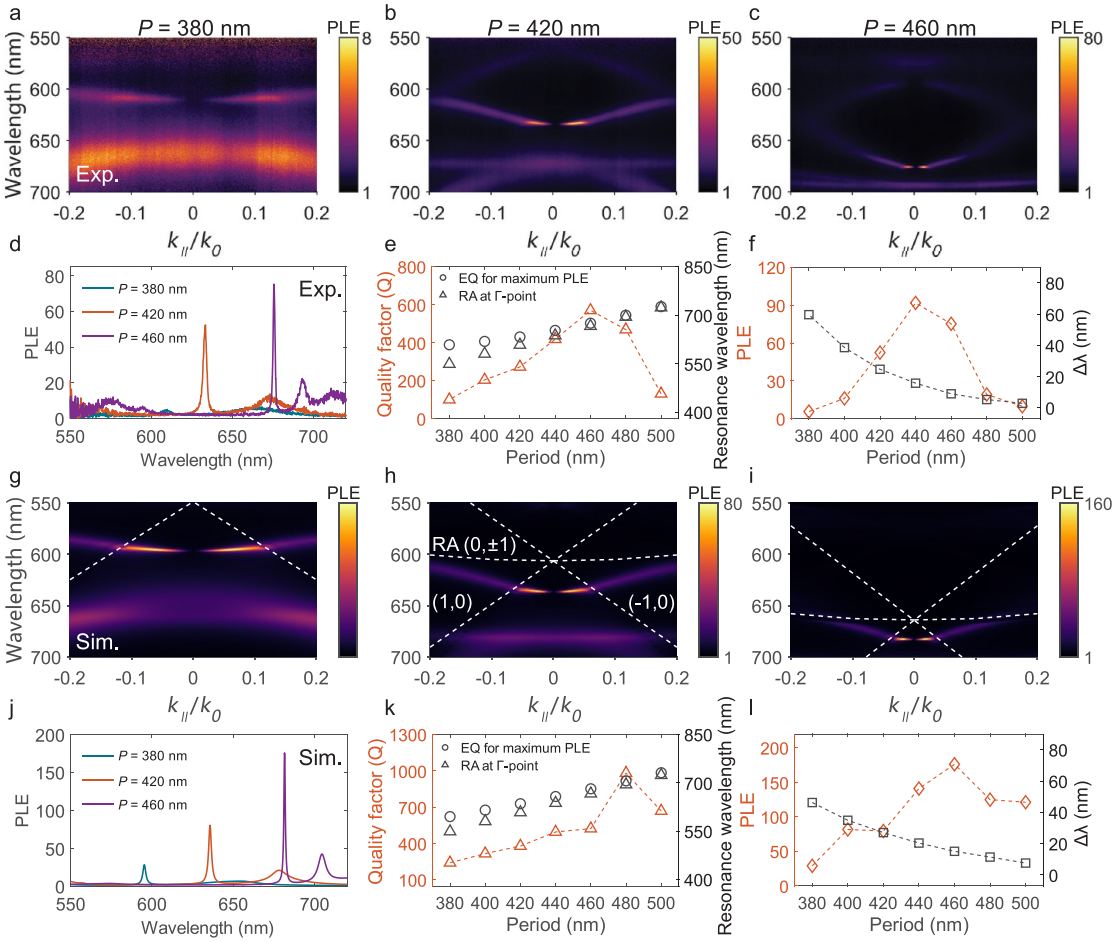

Figure 5. Lattice control of enhanced light emission. (a−c) The wave-vector resolved emission enhancement spectra measured at P = 380, 420, and 460 nm. (d) The emission spectra for quasi-BIC$_1$ obtained by cutting through the maximum PLE dispersion curves in panels a, b, and c. (e,f) Varying the periodicity of the square lattice to tune the quality factors (orange triangles in panel e) corresponding to the maximum of PLE (orange rhombus in panel f) in the dispersion for quasi-BIC$_1$. The black circles and triangles in panel e represent the resonance wavelengths for quasi-BIC$_1$ and RA, respectively, and the black squares in panel f represent their discrepancy ($\Delta\lambda$). (g−l) Simulation results corresponding to the measurements in panels a−f.

l) gradually decreases and approaches zero. This observation highlights the positive role of the resonance at the Γ-point in enhancing the near-field of quasi-BIC$_1$, which is achieved through the collective coupling of EQ modes of the silicon nanoparticles enhanced by in-plane diffraction (see the near-field plots in Figure S10). This amplifies the field confinement of quasi-BIC$_1$ and enhances the PL emission from the dye molecules in the surrounding environment. By employing the concept of collective resonances, we can elucidate the previously mentioned issue as well regarding the significant variations in field intensity between quasi-BIC$_1$ and quasi-BIC$_2$.

Considering the out-coupling efficiency of an extended emitting layer, we extracted the absorption enhancement of the emitters from the measured PLE data. Our PLE measurements show that in the off-resonance spectral region (Figure S8a), the PL is enhanced by a factor of 1.4−2.2 (Figure S8b). This enhancement arises from the excitation of localized Mie resonance at the nanoparticles.[28,30,31] The resonant energy is more effectively absorbed by the dye molecules, leading to increased PL. Accounting for this absorption enhancement, our study achieves a remarkable maximum out-coupling efficiency enhancement of ∼41-fold using quasi-BIC at a defined wave-vector of $k_{\parallel}/k_0 \sim 0.025$ ($\theta = 1.4°$). To the best of our knowledge, this directional emission enhancement represents one of the highest reported in the literature for extended emitting layers with a thickness beyond 100 nm (Supplementary Table S1).[23,28,30,31,39,41−46]

In summary, our work successfully achieves directionally enhanced vortex light emission from a layer of doped highly efficient molecules covering low-loss c-Si metasurfaces in the visible band. We extensively analyze and compare the mode properties of dual-BICs arising from EQ and MD$_z$ resonances in c-Si meta-atoms. The symmetric EQ resonance generates a highly enhanced near-field outside the c-Si nanodisks, leading to a significant increase in the optical LDOS of the extended emitting layer. Additionally, we show that the Q-factor of the EQ resonance-induced quasi-BIC can be finely tuned to 1000 in the visible band by coupling with RA, which further boosts the near-field spatial overlap with the emitters and the emission enhancement of quasi-BICs. Our findings have implications for developing lighting, lasing, and sensing devices.

■ ASSOCIATED CONTENT

Supporting Information

The Supporting Information is available free of charge at https://pubs.acs.org/doi/10.1021/acs.nanolett.3c02148.

https://doi.org/10.1021/acs.nanolett.3c02148
Nano Lett. 2023, 23, 7584−7592

Contents of sample fabrication, optical characterization, numerical simulations and multipole decomposition, absorption enhancement and wave-vector resolved PL spectra, near-field intensity enhancement for quasi-BIC, polarization vortex emission surrounding dual-BICs, comparison of directional emission enhancement characteristics with the reported results from literature (PDF)

AUTHOR INFORMATION

Corresponding Authors

Shaojun Wang − *School of Optoelectronic Science and Engineering & Collaborative Innovation Center of Suzhou Nano Science and Technology, Soochow University, Suzhou 215006, China; Key Lab of Advanced Optical Manufacturing Technologies of Jiangsu Province & Key Lab of Modern Optical Technologies of Education Ministry of China, Soochow University, Suzhou 215006, China;* orcid.org/0000-0002-0812-0782; Email: swang.opto@suda.edu.cn

Xiaofeng Li − *School of Optoelectronic Science and Engineering & Collaborative Innovation Center of Suzhou Nano Science and Technology, Soochow University, Suzhou 215006, China; Key Lab of Advanced Optical Manufacturing Technologies of Jiangsu Province & Key Lab of Modern Optical Technologies of Education Ministry of China, Soochow University, Suzhou 215006, China;* orcid.org/0000-0002-4115-3287; Email: xfl@suda.edu.cn

Authors

Zhenghe Zhang − *School of Optoelectronic Science and Engineering & Collaborative Innovation Center of Suzhou Nano Science and Technology, Soochow University, Suzhou 215006, China; Key Lab of Advanced Optical Manufacturing Technologies of Jiangsu Province & Key Lab of Modern Optical Technologies of Education Ministry of China, Soochow University, Suzhou 215006, China*

Chaojie Xu − *Institute of Functional Nano & Soft Materials (FUNSOM) and Jiangsu Key Laboratory for Carbon-Based Functional Materials Devices, Soochow University, Suzhou 215123, China*

Chen Liu − *School of Optoelectronic Science and Engineering & Collaborative Innovation Center of Suzhou Nano Science and Technology, Soochow University, Suzhou 215006, China; Key Lab of Advanced Optical Manufacturing Technologies of Jiangsu Province & Key Lab of Modern Optical Technologies of Education Ministry of China, Soochow University, Suzhou 215006, China*

Man Lang − *School of Optoelectronic Science and Engineering & Collaborative Innovation Center of Suzhou Nano Science and Technology, Soochow University, Suzhou 215006, China; Key Lab of Advanced Optical Manufacturing Technologies of Jiangsu Province & Key Lab of Modern Optical Technologies of Education Ministry of China, Soochow University, Suzhou 215006, China*

Yuehao Zhang − *School of Optoelectronic Science and Engineering & Collaborative Innovation Center of Suzhou Nano Science and Technology, Soochow University, Suzhou 215006, China; Key Lab of Advanced Optical Manufacturing Technologies of Jiangsu Province & Key Lab of Modern Optical Technologies of Education Ministry of China, Soochow University, Suzhou 215006, China*

Minghao Li − *Department of Physics and Swiss Nanoscience Institute, University of Basel, 4056 Basel, Switzerland*

Wanli Lu − *School of Materials Science and Physics, China University of Mining and Technology, Xuzhou 221116, China*

Zefeng Chen − *School of Optoelectronic Science and Engineering & Collaborative Innovation Center of Suzhou Nano Science and Technology, Soochow University, Suzhou 215006, China; Key Lab of Advanced Optical Manufacturing Technologies of Jiangsu Province & Key Lab of Modern Optical Technologies of Education Ministry of China, Soochow University, Suzhou 215006, China;* orcid.org/0000-0002-0689-8443

Chinhua Wang − *School of Optoelectronic Science and Engineering & Collaborative Innovation Center of Suzhou Nano Science and Technology, Soochow University, Suzhou 215006, China; Key Lab of Advanced Optical Manufacturing Technologies of Jiangsu Province & Key Lab of Modern Optical Technologies of Education Ministry of China, Soochow University, Suzhou 215006, China;* orcid.org/0000-0003-1025-3872

Complete contact information is available at: https://pubs.acs.org/10.1021/acs.nanolett.3c02148

Author Contributions

⊥Z.Z. and C.X. contributed equally to this work.

Notes

The authors declare no competing financial interest.

ACKNOWLEDGMENTS

We thank the discussions with Prof. Yadong Xu from our school of physical science and technology. This work was financially supported by the National Natural Science Foundation of China (62275184, 62274114, and 62120106001), Natural Science Foundation of Jiangsu Province (BK20200859 and BK20210713), and the Priority Academic Program Development (PAPD) of Jiangsu Higher Education Institutions.

REFERENCES

(1) Marinica, D.; Borisov, A.; Shabanov, S. Bound states in the continuum in photonics. *Phys. Rev. Lett.* **2008**, *100*, 183902.

(2) Hsu, C. W.; Zhen, B.; Stone, A. D.; Joannopoulos, J. D.; Soljačić, M. Bound states in the continuum. *Nat. Rev. Mater.* **2016**, *1*, 1−13.

(3) Yesilkoy, F.; Arvelo, E. R.; Jahani, Y.; Liu, M.; Tittl, A.; Cevher, V.; Kivshar, Y.; Altug, H. Ultrasensitive hyperspectral imaging and biodetection enabled by dielectric metasurfaces. *Nat. Photonics* **2019**, *13*, 390−396.

(4) Koshelev, K.; Kruk, S.; Melik-Gaykazyan, E.; Choi, J.-H.; Bogdanov, A.; Park, H.-G.; Kivshar, Y. Subwavelength dielectric resonators for nonlinear nanophotonics. *Science* **2020**, *367*, 288−292.

(5) Yin, X.; Jin, J.; Soljačić, M.; Peng, C.; Zhen, B. Observation of topologically enabled unidirectional guided resonances. *Nature* **2020**, *580*, 467−471.

(6) Ardizzone, V.; Riminucci, F.; Zanotti, S.; Gianfrate, A.; Efthymiou-Tsironi, M.; Suàrez-Forero, D.; Todisco, F.; De Giorgi, M.; Trypogeorgos, D.; Gigli, G.; Baldwin, K.; Pfeiffer, L.; Ballarini, D.; Nguyen, H. S.; Gerace, D.; Sanvitto, D. Polariton Bose−Einstein condensate from a bound state in the continuum. *Nature* **2022**, *605*, 447−452.

(7) Zhang, X.; Liu, Y.; Han, J.; Kivshar, Y.; Song, Q. Chiral emission from resonant metasurfaces. *Science* **2022**, *377*, 1215−1218.

(8) Kühner, L.; Sortino, L.; Berté, R.; Wang, J.; Ren, H.; Maier, S. A.; Kivshar, Y.; Tittl, A. Radial bound states in the continuum for polarization-invariant nanophotonics. *Nat. Commun.* **2022**, *13*, 4992.
(9) Chen, Y.; Deng, H.; Sha, X.; Chen, W.; Wang, R.; Chen, Y.-H.; Wu, D.; Chu, J.; Kivshar, Y. S.; Xiao, S.; Qiu, C.-W. Observation of intrinsic chiral bound states in the continuum. *Nature* **2023**, *613*, 474−478.
(10) Yang, G.; Dev, S. U.; Allen, M. S.; Allen, J. W.; Harutyunyan, H. Optical bound states in the continuum enabled by magnetic resonances coupled to a mirror. *Nano Lett.* **2022**, *22*, 2001−2008.
(11) Zhou, L.; Panmai, M.; Li, S.; Mao, Y.; He, W.; Huang, H.; Lan, S. Lighting up Si nanoparticle arrays by exploiting the bound states in the continuum formed in a Si/Au hybrid nanostructure. *ACS Photonics* **2022**, *9*, 2991−2999.
(12) Zhen, B.; Hsu, C. W.; Lu, L.; Stone, A. D.; Soljačić, M. Topological nature of optical bound states in the continuum. *Phys. Rev. Lett.* **2014**, *113*, 257401.
(13) Zhang, Y.; Chen, A.; Liu, W.; Hsu, C. W.; Wang, B.; Guan, F.; Liu, X.; Shi, L.; Lu, L.; Zi, J. Observation of polarization vortices in momentum space. *Phys. Rev. Lett.* **2018**, *120*, 186103.
(14) Koshelev, K.; Kivshar, Y. Dielectric resonant metaphotonics. *ACS Photonics* **2021**, *8*, 102−112.
(15) Doeleman, H. M.; Monticone, F.; den Hollander, W.; Alù, A.; Koenderink, A. F. Experimental observation of a polarization vortex at an optical bound state in the continuum. *Nat. Photonics* **2018**, *12*, 397−401.
(16) Plotnik, Y.; Peleg, O.; Dreisow, F.; Heinrich, M.; Nolte, S.; Szameit, A.; Segev, M. Experimental observation of optical bound states in the continuum. *Phys. Rev. Lett.* **2011**, *107*, 183901.
(17) Shi, T.; Deng, Z.-L.; Tu, Q.-A.; Cao, Y.; Li, X. Displacement-mediated bound states in the continuum in all-dielectric superlattice metasurfaces. *PhotoniX* **2021**, *2*, 1−10.
(18) Jin, J.; Yin, X.; Ni, L.; Soljačić, M.; Zhen, B.; Peng, C. Topologically enabled ultrahigh-Q guided resonances robust to out-of-plane scattering. *Nature* **2019**, *574*, 501−504.
(19) Koshelev, K.; Lepeshov, S.; Liu, M.; Bogdanov, A.; Kivshar, Y. Asymmetric metasurfaces with high-Q resonances governed by bound states in the continuum. *Phys. Rev. Lett.* **2018**, *121*, 193903.
(20) Kodigala, A.; Lepetit, T.; Gu, Q.; Bahari, B.; Fainman, Y.; Kanté, B. Lasing action from photonic bound states in continuum. *Nature* **2017**, *541*, 196−199.
(21) Ha, S. T.; Fu, Y. H.; Emani, N. K.; Pan, Z.; Bakker, R. M.; Paniagua-Domínguez, R.; Kuznetsov, A. I. Directional lasing in resonant semiconductor nanoantenna arrays. *Nat. Nanotechnol.* **2018**, *13*, 1042−1047.
(22) Huang, C.; Zhang, C.; Xiao, S.; Wang, Y.; Fan, Y.; Liu, Y.; Zhang, N.; Qu, G.; Ji, H.; Han, J.; Ge, L.; Kivshar, Y.; Song, Q. Ultrafast control of vortex microlasers. *Science* **2020**, *367*, 1018−1021.
(23) Kim, S.; Woo, B. H.; An, S.-C.; Lim, Y.; Seo, I. C.; Kim, D.-S.; Yoo, S.; Park, Q.-H.; Jun, Y. C. Topological control of 2D perovskite emission in the strong coupling regime. *Nano Lett.* **2021**, *21*, 10076−10085.
(24) Dang, N. H. M.; Zanotti, S.; Drouard, E.; Chevalier, C.; Trippé-Allard, G.; Amara, M.; Deleporte, E.; Ardizzone, V.; Sanvitto, D.; Andreani, L. C.; Seassal, C.; Gerace, D.; Nguyen, H. S. Realization of polaritonic topological charge at room temperature using polariton bound states in the continuum from perovskite metasurface. *Advanced Optical Materials* **2022**, *10*, 2102386.
(25) Wu, M.; Ha, S. T.; Shendre, S.; Durmusoglu, E. G.; Koh, W.-K.; Abujetas, D. R.; Sánchez-Gil, J. A.; Paniagua-Domínguez, R.; Demir, H. V.; Kuznetsov, A. I. Room-temperature lasing in colloidal nanoplatelets via Mie-resonant bound states in the continuum. *Nano Lett.* **2020**, *20*, 6005−6011.
(26) Azzam, S. I.; Chaudhuri, K.; Lagutchev, A.; Jacob, Z.; Kim, Y. L.; Shalaev, V. M.; Boltasseva, A.; Kildishev, A. V. Single and Multi-Mode Directional Lasing from Arrays of Dielectric Nanoresonators. *Laser & Photonics Reviews* **2021**, *15*, 2000411.
(27) Mohamed, S.; Wang, J.; Rekola, H.; Heikkinen, J.; Asamoah, B.; Shi, L.; Hakala, T. K. Controlling topology and polarization state of lasing photonic bound states in continuum. *Laser & Photonics Reviews* **2022**, *16*, 2100574.
(28) Lozano, G.; Louwers, D. J.; Rodríguez, S. R.; Murai, S.; Jansen, O. T.; Verschuuren, M. A.; Gómez Rivas, J. Plasmonics for solid-state lighting: enhanced excitation and directional emission of highly efficient light sources. *Light: Science & Applications* **2013**, *2*, e66−e66.
(29) Guo, K.; Du, M.; Osorio, C. I.; Koenderink, A. F. Broadband light scattering and photoluminescence enhancement from plasmonic Vogel's golden spirals. *Laser & Photonics Reviews* **2017**, *11*, 1600235.
(30) Wang, S.; Le-Van, Q.; Peyronel, T.; Ramezani, M.; Van Hoof, N.; Tiecke, T. G.; Gomez Rivas, J. Plasmonic nanoantenna arrays as efficient etendue reducers for optical detection. *ACS Photonics* **2018**, *5*, 2478−2485.
(31) Murai, S.; Castellanos, G. W.; Raziman, T.; Curto, A. G.; Rivas, J. G. Enhanced light emission by magnetic and electric resonances in dielectric metasurfaces. *Advanced Optical Materials* **2020**, *8*, 1902024.
(32) Sell, D.; Yang, J.; Doshay, S.; Zhang, K.; Fan, J. A. Visible light metasurfaces based on single-crystal silicon. *ACS Photonics* **2016**, *3*, 1919−1925.
(33) Zhou, Z.; Li, J.; Su, R.; Yao, B.; Fang, H.; Li, K.; Zhou, L.; Liu, J.; Stellinga, D.; Reardon, C. P.; Krauss, T. F.; Wang, X. Efficient silicon metasurfaces for visible light. *ACS Photonics* **2017**, *4*, 544−551.
(34) Zhang, C.; Xu, Y.; Liu, J.; Li, J.; Xiang, J.; Li, H.; Li, J.; Dai, Q.; Lan, S.; Miroshnichenko, A. E. Lighting up silicon nanoparticles with Mie resonances. *Nat. Commun.* **2018**, *9*, 1−7.
(35) Zhang, Z.; Liu, P.; Lu, W.; Bai, P.; Zhang, B.; Chen, Z.; Maier, S. A.; Rivas, J. G.; Wang, S.; Li, X. High-Q collective Mie resonances in monocrystalline silicon nanoantenna arrays for the visible light. *Fundamental Research* **2022**, DOI: 10.1016/j.fmre.2022.05.020.
(36) Naren, G.; Hsu, C.-W.; Li, S.; Morimoto, M.; Tang, S.; Hernando, J.; Guirado, G.; Irie, M.; Raymo, F. M.; Sundén, H.; Andréasson, J. An all-photonic full color RGB system based on molecular photoswitches. *Nat. Commun.* **2019**, *10*, 3996.
(37) Sadrieva, Z.; Frizyuk, K.; Petrov, M.; Kivshar, Y.; Bogdanov, A. Multipolar origin of bound states in the continuum. *Phys. Rev. B* **2019**, *100*, 115303.
(38) Rodriguez, S.; Lozano, G.; Verschuuren, M.; Gomes, R.; Lambert, K.; De Geyter, B.; Hassinen, A.; Van Thourhout, D.; Hens, Z.; Gómez Rivas, J. Quantum rod emission coupled to plasmonic lattice resonances: A collective directional source of polarized light. *Appl. Phys. Lett.* **2012**, *100*, 111103.
(39) Ramezani, M.; Lozano, G.; Verschuuren, M. A.; Gómez-Rivas, J. Modified emission of extended light emitting layers by selective coupling to collective lattice resonances. *Phys. Rev. B* **2016**, *94*, 125406.
(40) Bin-Alam, M. S.; Reshef, O.; Mamchur, Y.; Alam, M. Z.; Carlow, G.; Upham, J.; Sullivan, B. T.; Ménard, J.-M.; Huttunen, M. J.; Boyd, R. W.; Dolgaleva, K. Ultra-high-Q resonances in plasmonic metasurfaces. *Nat. Commun.* **2021**, *12*, 974.
(41) Vaskin, A.; Bohn, J.; Chong, K. E.; Bucher, T.; Zilk, M.; Choi, D.-Y.; Neshev, D. N.; Kivshar, Y. S.; Pertsch, T.; Staude, I. Directional and spectral shaping of light emission with Mie-resonant silicon nanoantenna arrays. *ACS Photonics* **2018**, *5*, 1359−1364.
(42) Hasebe, H.; Sugimoto, H.; Hinamoto, T.; Fujii, M. Coupled toroidal dipole modes in silicon nanodisk metasurface: polarization independent narrow band absorption and directional emission. *Advanced Optical Materials* **2020**, *8*, 2001148.
(43) Joo, W.-J.; Kyoung, J.; Esfandyarpour, M.; Lee, S.-H.; Koo, H.; Song, S.; Kwon, Y.-N.; Song, S. H.; Bae, J. C.; Jo, A.; Kwon, M.-J.; Han, S. H.; Kim, S.-H.; Hwang, S.; Brongersma, M. L. Metasurface-driven OLED displays beyond 10,000 pixels per inch. *Science* **2020**, *370*, 459−463.
(44) Mao, P.; Liu, C.; Li, X.; Liu, M.; Chen, Q.; Han, M.; Maier, S. A.; Sargent, E. H.; Zhang, S. Single-step-fabricated disordered metasurfaces for enhanced light extraction from LEDs. *Light: Science & Applications* **2021**, *10*, 180.
(45) Liu, T.; Yang, C.; Fan, Z.; Chen, X.; Chen, Z.; Su, Y.; Zhu, H.; Sun, F.; Jiang, T.; Zhu, W.; Shen, W.; He, J.; Zhu, H.; Liu, X.; Yang, Y. M. Spectral narrowing and enhancement of directional emission of

https://doi.org/10.1021/acs.nanolett.3c02148
Nano Lett. 2023, 23, 7584−7592

perovskite light emitting diode by microcavity. *Laser & Photonics Reviews* **2022**, *16*, 2200091.
(46) Carreño, J. M.; Passarelli, N.; Otero-Martínez, C.; Polavarapu, L.; Pérez, L. A.; Reparaz, J. S.; Alonso, M. I.; Mihi, A. Enhanced Photoluminescence of Cesium Lead Halide Perovskites by Quasi-3D Photonic Crystals. *Advanced Optical Materials* **2022**, *10*, 2101324.

https://doi.org/10.1021/acs.nanolett.3c02148
Nano Lett. 2023, 23, 7584−7592

Supporting Information

Dual control of enhanced quasi-bound states in the continuum emission from resonant c-Si metasurfaces

Zhenghe Zhang,[†,‡,⊥] Chaojie Xu,[¶,⊥] Chen Liu,[†,‡] Man Lang,[†,‡] Yuehao Zhang,[†,‡] Minghao Li,[§] Wanli Lu,[‖] Zefeng Chen,[†,‡] Chinhua Wang,[†,‡] Shaojun Wang,[*,†,‡] and Xiaofeng Li[*,†,‡]

† School of Optoelectronic Science and Engineering & Collaborative Innovation Center of Suzhou Nano Science and Technology, Soochow University, Suzhou 215006, China

‡ Key Lab of Advanced Optical Manufacturing Technologies of Jiangsu Province & Key Lab of Modern Optical Technologies of Education Ministry of China, Soochow University, Suzhou 215006, China

¶ Institute of Functional Nano & Soft Materials (FUNSOM) and Jiangsu Key Laboratory for Carbon-Based Functional Materials Devices, Soochow University, Suzhou 215123, China

§ Department of Physics and Swiss Nanoscience Institute, University of Basel, Klingelbergstrasse 82, 4056 Basel, Switzerland

‖ School of Materials Science and Physics, China University of Mining and Technology, Xuzhou 221116, China

⊥ The authors contributed equally to this work

*E-mail: swang.opto@suda.edu.cn; xfl@suda.edu.cn

Contents:

S1 Sample fabrication

The monocrystalline silicon (c-Si) metasurfaces were fabricated on SOI wafers (ShinEtsu Inc.) using a "floating off" technique to transfer the nanoparticle arrays (NPAs) onto transparent quartz substrates (Figure S1).[1] The fabrication process involved dry etching of c-Si NPAs on SOI wafers using electron beam lithography (EBL) patterning. A ~500 nm thick polymethyl methacrylate (PMMA) layer was then coated on the NPA. The sample was immersed in hydrofluoric acid (HF) to etch the oxide layer of SOI, followed by transfer to deionized water. The c-Si NPAs enclosed in the PMMA slab floated on the water surface, and the soft PMMA slab was placed onto a quartz substrate. After drying in the ambient environment, the PMMA slab adhered to the quartz by baking the sample on a hotplate at 160 ℃ for 15 minutes. The PMMA slab was removed by immersing the sample in acetone and ethanol, resulting in the c-Si metasurfaces on quartz. Finally, another 300 nm thick PMMA slab doped with 0.1 wt% DAEr dye was spin-coated onto the metasurface. The fluorescent dye was synthesized following the recipe described in the literature.[2]

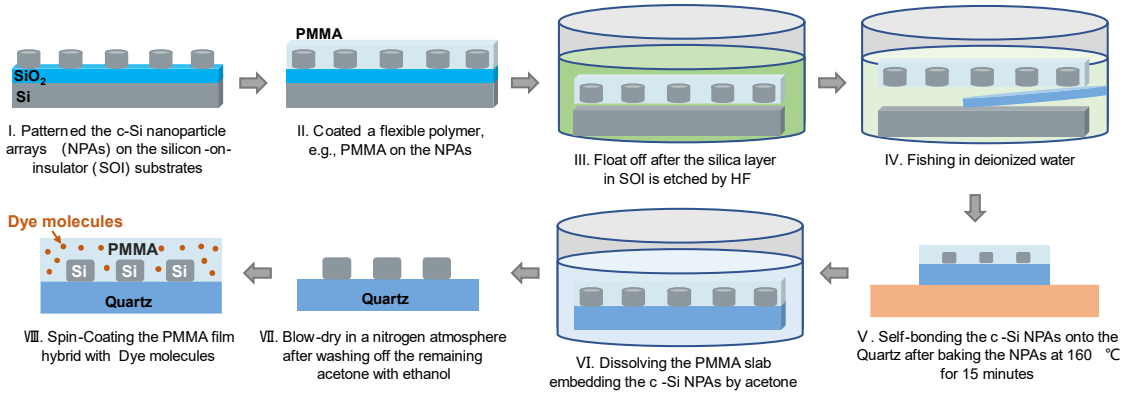

Figure S1 Schematic of the fabrication processes for preparing emitting metasurfaces combing c-Si nanoparticle arrays and highly efficient dye molecules.

S2 Optical characterizations

We employed a home-built Fourier imaging setup (Figure S2), integrated with an inverted microscope (Nikon Ti_2-U) equipped with a pair of objectives with the same optical parameters (Plan Fluor ELWD 60x, NA = 0.7, Nikon), to measure the extinction dispersion curves. The extinction spectrum of the sample is given by $1-T/T_{\text{reference}}$, with T being transmission into forward direction from the NPA, and $T_{\text{reference}}$ is from the bare dye film. The collimated white-

light beam was focused onto the sample through the objective (OL_1), and the transmitted light was collected by the second objective (OL_2). A Fourier lens (FL) replicated the back focal plane image (Fourier image) of the objective (OL_2) to infinity. A tube lens (TL) focused this image onto the slit of the spectrometer (Shemrock 500i), which was coupled to an electron-multiplying charge-coupled device camera (EMCCD, iXon Ultra 888). A linear polarizer between the FL and TL determined the polarization of the light beam.

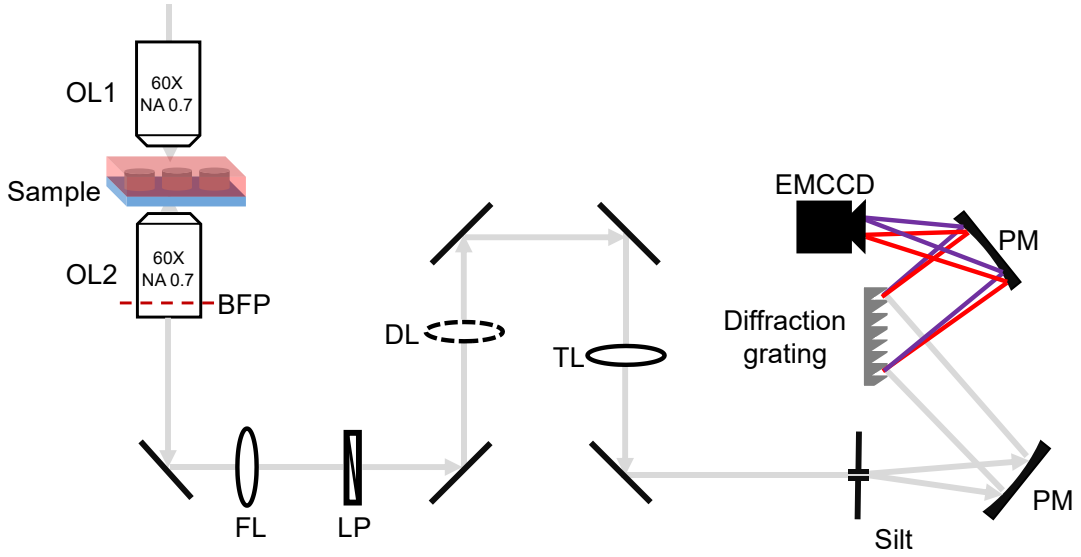

Figure S2 Schematic of Fourier imaging setup for extinction dispersion curves measurement. OL: objective lens, FL: Fourier Lens, DL: delayed lens, TL: tube lens, LP: linear polarizer, PM: parabolic mirror, NA: numerical aperture, BFP: back focal plane.

We carried out the PL dispersion using another Fourier setup (Figure S3). The sample was illuminated by a blue LED, and its spectrum was cut by a band-pass filter with a center wavelength of 450 nm and a line width of 10 nm. The emitted and scattered light from the sample was collected by the objective (OL) and filtered by a long-pass filter before being sent into the spectrometer. The emitted light with the selected wavelength was analyzed in the Fourier space. We continued to quantitatively investigate the emission pattern using the technique of Fourier imaging, i.e., back-focal-plane imaging. An objective with NA = 0.7 was used to collect the emission from the sample. An additional pair of lenses copied and sent the back-focal-plane image inside the body of the objective to the EMCCD. The PL intensity distribution PL (k_x/k_0, k_y/k_0) recorded at the back-focal-plane of the objective was transformed into the angular distribution of the PL intensity PL (θ, ϕ) following the equations:[3]

$$PL(k_x/k_0, k_y/k_0) = PL(\theta, \phi)\cos^{-1}\theta \quad (1)$$

$$k_x = \sin\theta\cos\phi \quad (2)$$

$$k_y = \sin\theta\sin\phi \quad (3)$$

where the standard apodization factor $\cos^{-1}\theta$ in equation (2) is introduced to preserve the projected energy on the back-focal-plane,[4] k_0 represents the wave-vector in free space, and θ and ϕ correspond to the elevation and azimuth angles defined in spherical coordinates, respectively. The maximum elevation angle θ for collecting the PL is determined by the numerical aperture (NA) of the objective.

Its polarization is analyzed in terms of Stokes parameters (S_0, S_1, S_2, and S_3) by rotating a quarter-wave plate (QWP) relative to a fixed polarizer in front of the detector. For each given angle β of the QWP, the intensity of the emission signal can be calculated as a function of Stokes parameters as,[5]

$$I(\beta, \delta) = \frac{1}{2}\{S_0 - (S_1\cos 2\beta - S_2\sin 2\beta)\cos 2\beta + [(S_2\cos 2\beta - S_1\sin 2\beta)\cos\delta + S_3\sin\delta]\sin 2\beta\} \quad (4)$$

where δ is the phase retardation angle of the QWP, the dispersion of which is calibrated by Thorlabs. The intensities here were recorded with the QWP rotated every 10° from 0° to 180°. This leads to an overdetermined equation system consisting of nineteen equation sets for solving four unknown parameters (S_0, S_1, S_2, and S_3). This approach minimizes the random errors for determining the azimuthal angle of QWP and polarizer. Consequently, it improves the accuracy of the polarization analysis. After obtaining the Stokes parameters, we can calculate the orientation angle ψ [$\psi = \frac{1}{2}\arctan(\frac{S_2}{S_1})$, $-\frac{\pi}{2} \le \psi \le \frac{\pi}{2}$] and the ellipticity angle χ [$\chi = \frac{1}{2}\arcsin(\frac{S_3}{S_0})$, $-\frac{\pi}{4} \le \chi \le \frac{\pi}{4}$] of polarization ellipse.

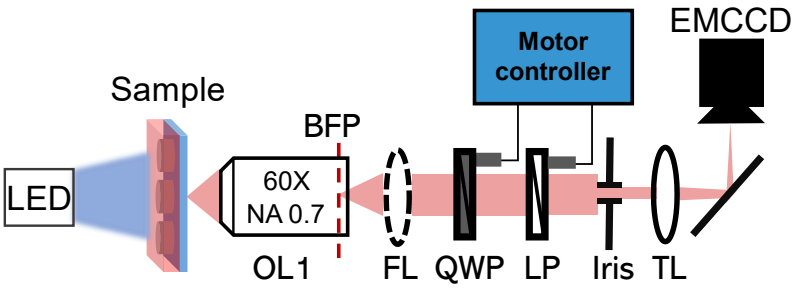

Figure S3 Schematic of Fourier imaging setup for measuring PL dispersion curves and Stokes parameters in momentum space. QWP: quarter-wave plate.

S3 Numerical simulations and multipole decomposition

Numerical simulations. All simulation data were obtained using a finite-difference time-domain (FDTD) solver with the commercial package Lumerical. Plane waves were used to excite both extinction dispersion and near-field simulations. To simulate an infinite array, a single cell was employed with Bloch boundary conditions set in the in-plane direction. The refractive index and absorption coefficients of c-Si were determined using an ellipsometer.[1] The quartz substrate and PMMA were considered non-dispersive media with refractive indices of 1.45 and 1.49, respectively. Additionally, the multipole decomposition approach was applied to determine the Cartesian components of multipoles within the nanodisks based on near-field calculations.

Angle-dependent emission spectra were simulated based on the Lorentz reciprocity theorem.[6,7] Specifically, we calculated the enhancement factors of the electric field intensity in the molecules on the structure compared to off the structure. The metasurface was excited by a plane wave in the same direction as the measured emission signals. Considering the random distribution of molecular dipole orientations, the directional emission enhancement [$IE(\lambda, \theta, \phi)$] of the dipole sources was proportional to the calculated field intensity enhancement factors,

$$IE(\lambda, \theta, \phi) = \frac{\int_V |E(x, y, z, \lambda, \theta, \phi)|^2 \mathrm{d}V}{\int_V |E_{ref}(x, y, z, \lambda, \theta, \phi)|^2 \mathrm{d}V} \tag{5}$$

where λ is the wavelength. The volume integrals specifically consider the region outside the c-Si disk within a unit cell of the square lattice.

Multipole decomposition. To assess the characteristics of different Mie scattering modes produced by the polarization of the c-Si metasurface under optical fields, we determine the Cartesian components of the multipoles excited within the nanoparticles using multipole decomposition with TE polarization. We employ FDTD to capture the electric field amplitude $\boldsymbol{E}$ within a unit cell of the metasurface under excitation by a plane wave. From this data, we calculate the scattering current density induced in the particles by the incident field, as expressed by the following equation

$$\boldsymbol{J} = -i\omega\varepsilon_0(\varepsilon - \varepsilon_d)\boldsymbol{E} \tag{6}$$

Based on the scattering current density on the Cartesian basis, we calculate the electric, magnetic, toroidal dipole moments ($p_\alpha,\ m_\alpha,\ T_\alpha$), quadrupolar moments ($Q^e_{\alpha\beta},\ Q^m_{\alpha\beta},\ Q^T_{\alpha\beta}$),:

$$p_\alpha = \frac{i}{\omega}\int_V j_\alpha d^3r \tag{7}$$

$$m_\alpha = \frac{1}{2}\int_V (\boldsymbol{r}\times\boldsymbol{j})_\alpha d^3r \tag{8}$$

$$T_\alpha = \frac{1}{10}\int_V [(\boldsymbol{j}\cdot\boldsymbol{r})r_\alpha - 2r^2 j_\alpha]\, d^3r \tag{9}$$

$$Q^e_{\alpha\beta} = \frac{i}{\omega}\int_V [r_\alpha j_\beta + r_\beta j_\alpha - \frac{2}{3}\delta_{\alpha\beta}(\boldsymbol{r}\times\boldsymbol{j})]\, d^3r \tag{10}$$

$$Q^m_{\alpha\beta} = \frac{1}{3}\int_V [(\boldsymbol{r}\times\boldsymbol{j})_\alpha r_\beta + (\boldsymbol{r}\times\boldsymbol{j})_\beta r_\alpha]\, d^3r \tag{11}$$

$$Q^T_{\alpha\beta} = \frac{1}{42}\int_V [4(\boldsymbol{r}\cdot\boldsymbol{j})r_\alpha r_\beta + 2(\boldsymbol{j}\cdot\boldsymbol{r})r^2\delta_{\alpha\beta} - 5r^2(r_\alpha j_\beta + r_\beta j_\alpha)]\, d^3r \tag{12}$$

where the spatial position in Cartesian coordinates is defined by $\boldsymbol{r}$, so that α (or β) refers to x, y, z. In addition, we also consider the mean-square radii of the dipole or quadrupole ($M_a^{\langle 2\rangle},\ T_a^{\langle 2\rangle},\ Q_{\alpha\beta}^{m\langle 2\rangle}$) distributions:

$$M_a^{\langle 2\rangle} = \frac{iw}{20}\int_V r^2(\boldsymbol{r}\times\boldsymbol{j})_\alpha\, d^3r \tag{13}$$

$$T_a^{\langle 2\rangle} = \frac{1}{280}\int_V [3r^4 j_\alpha - 2r^2(\boldsymbol{r}\cdot\boldsymbol{j})r_\alpha]\, d^3r \tag{14}$$

$$Q_{\alpha\beta}^{m\langle 2\rangle} = \frac{i\omega}{42}\int_V r^2[(\boldsymbol{r}\times\boldsymbol{j})_\alpha r_\beta + (\boldsymbol{r}\times\boldsymbol{j})_\beta r_\alpha]d^3r \tag{15}$$

Subsequently, we can calculate the scattering cross-section for the electric/magnetic dipole and quadrupole resonances for the c-Si metasurface by the following equations:[1]

$$C_{sca}^{ED} = \frac{k_0^4}{6\pi\varepsilon_0^2 E_0^2}\sum_\alpha |p_\alpha + \frac{ik_0\varepsilon_d}{c}T_\alpha + \frac{ik_0^3\varepsilon_d^2}{c}T_\alpha^{\langle 2\rangle}|^2 \tag{16}$$

$$C_{sca}^{MD} = \frac{\eta_0^2 k_0^4 \varepsilon_d}{6\pi E_0^2}\sum_\alpha |m_\alpha + \frac{ik_0\varepsilon_d}{c}M_\alpha^{\langle 2\rangle}|^2 \tag{17}$$

$$C_{sca}^{EQ} = \frac{k_0^6\varepsilon_d}{80\pi\varepsilon_0^2 E_0^2}\sum_{\alpha\beta} |Q^e_{\alpha\beta} + \frac{ik_0\varepsilon_d}{c}Q^T_{\alpha\beta}|^2 \tag{18}$$

$$C_{sca}^{MQ} = \frac{\eta_0^2 k_0^6 \varepsilon_d^2}{80\pi E_0^2}\sum_{\alpha\beta} |Q^m_{\alpha\beta} + \frac{ik_0\varepsilon_d}{c}Q^{m\langle 2\rangle}_{\alpha\beta}|^2 \tag{19}$$

where $\boldsymbol{E}_0$, $\boldsymbol{k}_0$ are the electric field amplitude and wave vector of the incident wave, respectively, and η_0 is the impedance of free space.

The scattering cross-section of the multipole under TE polarization is depicted in Figure S4. Panel **a** presents the normalized total scattering intensity, while panels **b-f** illustrate the ED_y, MD_x, MD_z, MQ, and EQ resonances, respectively. These results align with Figures 2g and h in

the main text. Quasi-BIC_1 arises from the combined scattering contributions of EQ, MQ, and ED_y resonances, with EQ being the dominant component. Quasi-BIC_2 primarily originates from the MD_z resonances, with negligible scattering contributions from MQ and ED_y.

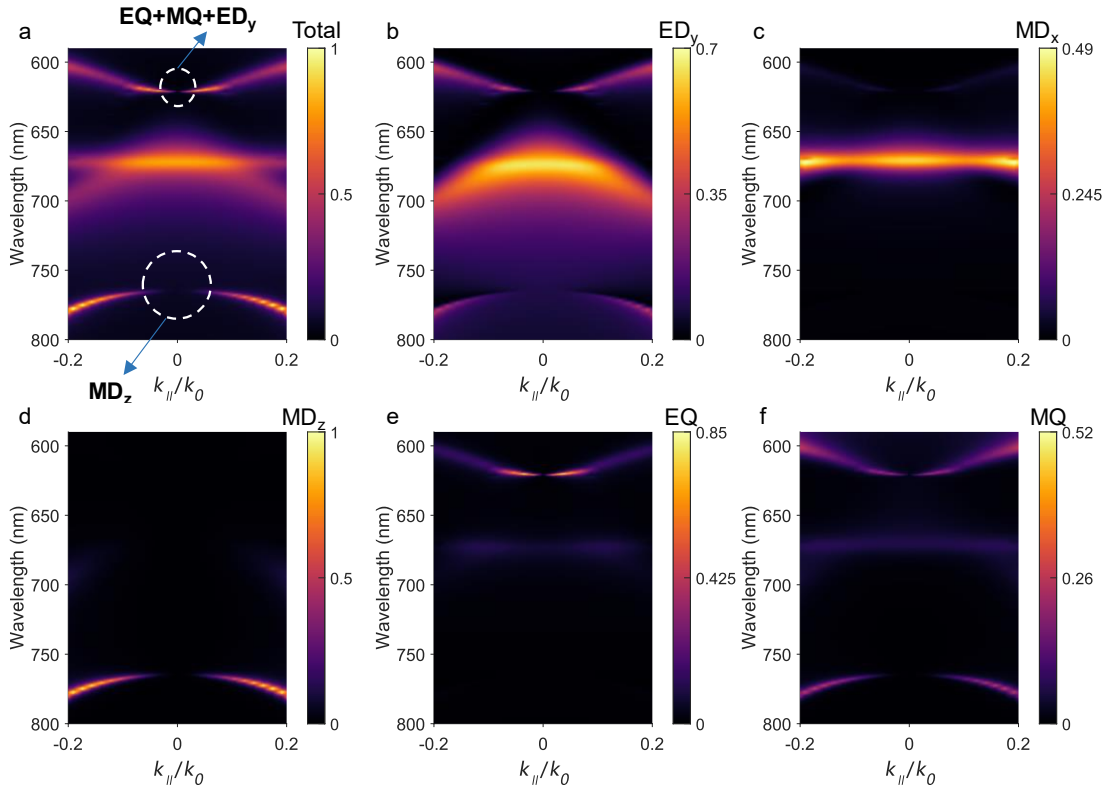

Figure S4 Multipole decomposition. Normalized scattering cross-sections of multipole of samples with D = 200 nm and P = 405 nm under TE polarization, including the total scattering intensity (a), the scattering cross-section of ED_y (b), MD_x (c), MD_z (d), EQ (e), and MQ (f), respectively. The BIC_1 is marked by white-dashed circle in panel a from the scattering contributions of EQ, MQ, and ED_y, while the BIC_2 is indicated by white-dashed circle at long wavelength from the scattering contributions of MD_z, MQ, and ED_y.

S4 Absorption enhancement and wave-vector resolved PL spectra

To validate the measurement of the PL dispersion curve and the calculation of PL enhancement (PLE), we extracted the raw PL intensity spectra from the peak PLE at $k_{||}/k_0$ = 0.05 (Figure 4a). These spectra include the light-emitting metasurface and the bare dye film, as shown in Figure S5. At the quasi-BIC emission peak (λ = 623 nm), the photon counts for the metasurfaces and the bare dye film are 29540 and 6816 (magnified 10×), respectively. The measured maximum PLE is ~44 fold, aligning with the data presented in Figure 4c.

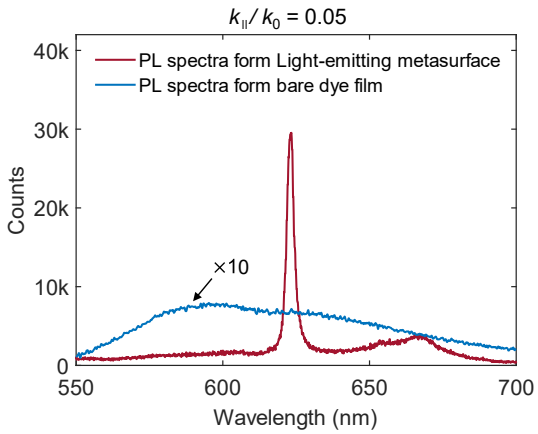

Figure S5 PL intensity spectra of the emission from metasurface (red) and bare dye film (blue, magnified 10×) taken from PL dispersion curves at $k_{||}/k_0 = 0.05$.

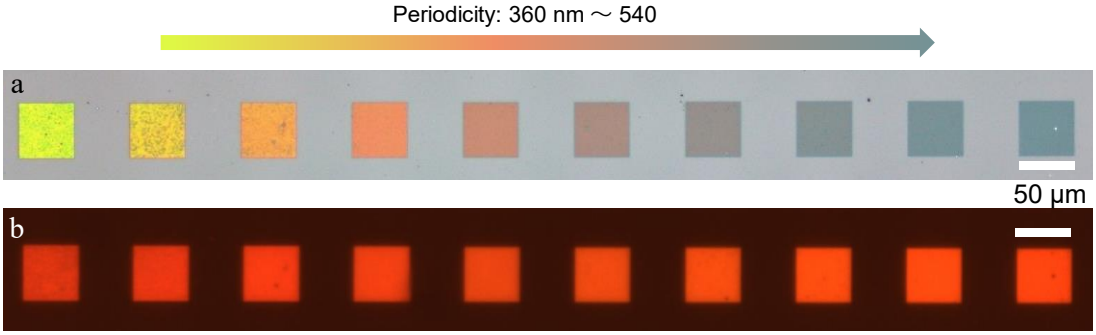

Figure S6 The bright-field microscope image **(a)** and PL image **(b)** of array samples with fixed *D* of 200 nm and varying *P* from 360 to 540 nm. Scale bars: 50 μm.

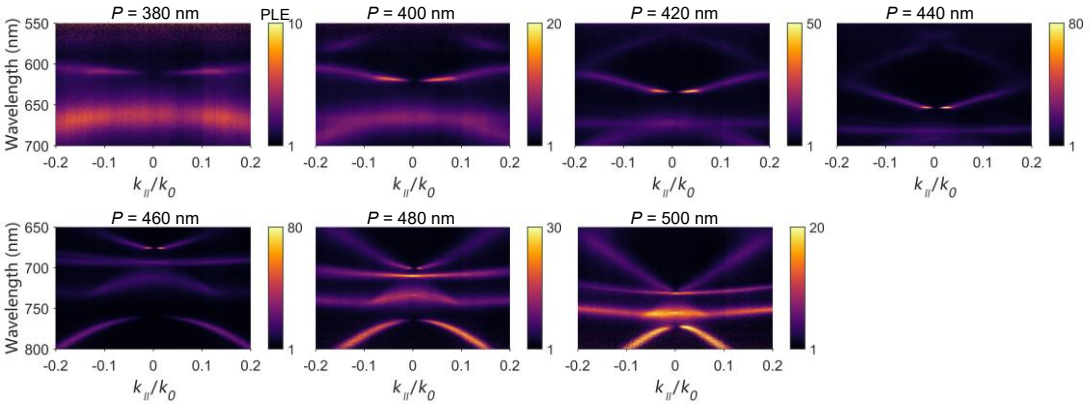

Figure S7 The wave-vector resolved PL spectra measurements of samples with fixed *D* of 200 nm and varying *P* from 360 to 540 nm.

The out-coupling efficiency of the extended emitting layer is influenced not only by the resonance metasurfaces but also by the absorption enhancement of the emitters to the pump beam. This enhancement is achieved through the excitation of localized Mie resonances on the nanoparticles using a focused pump beam at a center wavelength of 450 nm. The absorption enhancement can be quantified by analyzing the off-resonance spectral region in the PLE

spectrum, as depicted in Figure S8a. The off-resonance spectra in the range of 620-660 nm indicate the extent of absorption enhancement of the emitters. The absorption enhancement factors for different periods range from approximately 1.4 to 2.2, as summarized in Figure S8b.

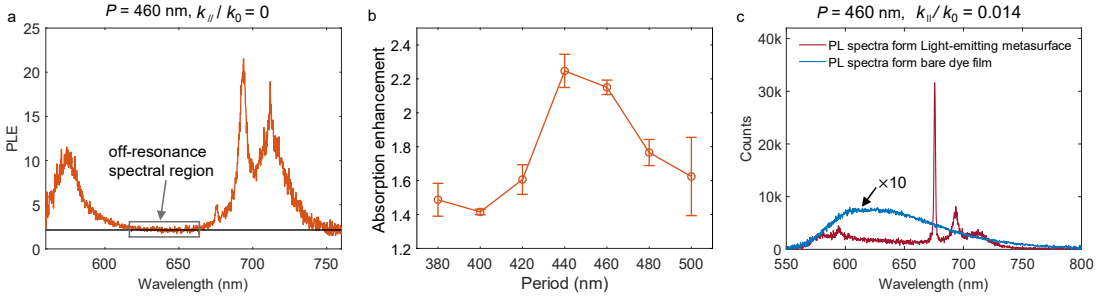

Figure S8 Pump absorption enhancement analysis. (a) PLE spectra taken from samples with P = 460 nm under normal incidence, the gray dashed box represents the off-resonant spectral region; (b) Absorption enhancement at P = 380-500 nm, equivalent to average PLE of the off-resonant spectral region; (c) PL intensity spectra of the emission from metasurface (red) and bare dye film (blue, magnified 10×) from PL dispersion curves at $k_{||}/k_0$ = 0.014.

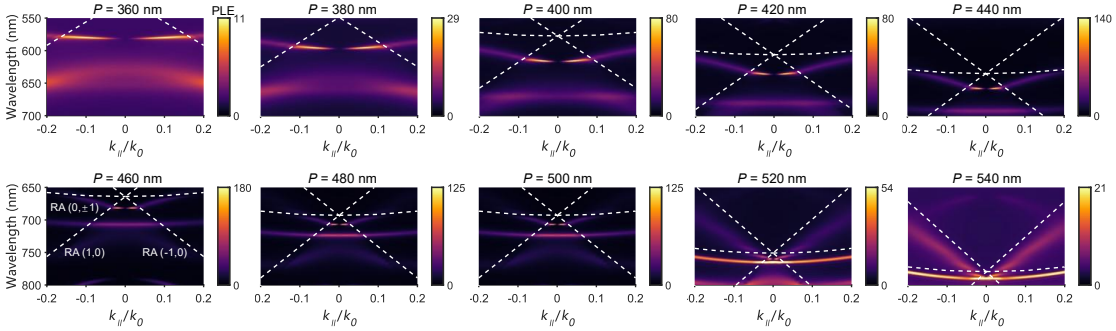

Figure S9 The wave-vector resolved PL spectra simulation of samples with fixed D of 200 nm and varying P from 360 to 540 nm.

S5 Near-field intensity enhancement for quasi-BICs

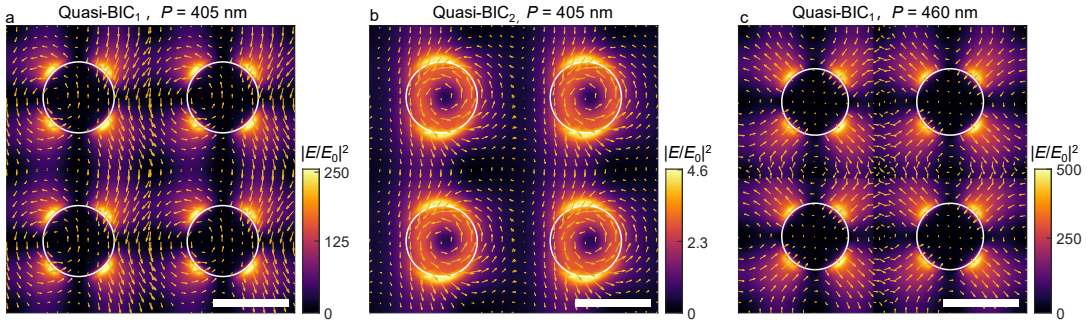

Figure S10 Multipole field intensity enhancement of quasi-BIC_1 and quasi-BIC_2. Top view of field intensity enhancement in the lattice for quasi-BIC_1 (a) and quasi-BIC_2 (b) at P = 405 nm, as well as quasi-BIC_1 at P = 460 nm (c). Scale bars: 202.5 nm (a), 202.5 (b), and 230 nm (c).

S6 Polarization vortex emission surrounding dual-BICs

We have obtained efficient quasi-BIC emission through multipole and lattice control. Here, we investigate the polarization vortex emission of quasi-BICs in wave-vector space. To accomplish this, we employed a PL Fourier imaging setup, as depicted in Figure S3, to measure the Stokes parameters of the PL emission in the *k*-space. The intensity distributions of quasi-BICs in *k*-space are recorded using filters with central wavelengths of λ = 621 nm and 765 nm and a bandwidth of 10 nm. By optimizing the measurements of the Stokes parameters (see the details in S2), we can determine the polarization state of the emitted light at different frequencies. We calculate the normalized total PL intensity distribution S_0 for BIC_1 and BIC_2 in the wave-vector space. Figures 3a and e show that both BICs exhibit a "donut" intensity distribution. At the polarization singularity (i.e., Γ-point, $k_x = k_y = 0$), where BICs are completely decoupled from the radiative continuum in free space and no far-field emission is generated, they exhibit a dark state. When departing from the Γ-point, the region corresponding to the quasi-BICs demonstrates a balanced radiation characteristic, indicating the features of symmetry-protected BICs. Additionally, we calculate the near-field intensity distribution in the wave-vector space for both types of quasi-BICs using the reciprocity theorem in FDTD, which is presented in the subsequent row of experimental results. All the salient features observed in the experiment are reproduced in the simulation results. Quasi-BIC_1 exhibits a total intensity of S_0 that is surrounded by four Rayleigh anomaly band lobes (indicated by white-dashed curves in the simulation data of Figure 3a), resulting in a roughly square-shaped far-field radiation pattern.

We then shift our focus to the polarization characteristics of the bright ring surrounding the BICs. Both BIC_1 and BIC_2 exhibit intensity distributions in S_1/S_0 and S_2/S_0, indicating linear polarization in specific directions, namely, fully linear polarization in the horizontal, vertical, 45°, and 135° directions. Notably, both types of quasi-BICs display the same polarization direction in S_1/S_0. However, in S_2/S_0, they exhibit opposite polarization states in the diagonal directions. The red region along the 45° polarization direction for BIC_1 corresponds to the blue region along the 135° polarization direction for BIC_2 in S_2/S_0, indicating the presence of linear vortex features of the two BICs in different directions.

To determine the direction of the polarization vortex of the quasi-BICs, we calculate the directional angle ψ of the polarization state using the equation $\psi = (1/2)\arctan(S_2/S_1)$ and present it in Figures 3d and h. In the plot, the extreme value of ψ is represented in black, while the range of directional angles from 0° to 180° is depicted using red and blue colors. The white region corresponding to the Γ-point in wave-vector space indicates an undefined value of "NAN", suggesting the uncertainty of the BICs' polarization at the Γ-point. Furthermore, the simulation results illustrate the vortex variation of linear polarization using grey double arrows. The polarizations of quasi-BIC_1 and quasi-BIC_2 complete one periodic rotation around a polarization singularity and return to the origin, demonstrating clear topological polarization characteristics. Thus, both of these quasi-BICs possess topological charges. The topological charges of BIC_1 and BIC_2 are calculated as -1 and $+1$, respectively, using the equation $q = \frac{1}{2\pi}\oint_C d\boldsymbol{k} \cdot \nabla\boldsymbol{\psi}$,[8] as the polarization vector of the two BICs rotates around the singularity in opposite directions.

In addition, we investigated the circular polarization characteristics by measuring and simulating S_3/S_0, which represents the degree of circular polarization, and the ellipticity χ. Due to the fully C_2 symmetric nature of the metasurfaces, the PL emission from the two symmetry-protected BICs is predominantly linearly polarized without circular polarization components. This results in a very small value of 0.1 for S_3/S_0 (Figures S11a and d), probably due to the mirror symmetry breaking of the structure under oblique incident angle. The ellipticity, χ, calculated from the experimental results by $\chi = (1/2)\arcsin(S_3/S_0)$, also indicates a weak polarization distribution for both BICs, as shown in Figures S11b and e. Similarly, the simulation results demonstrate an undetermined polarization state at the Γ-point representing the BICs, with a negligible circular polarization component observed in the vicinity of the BICs (Figures S11c and f).

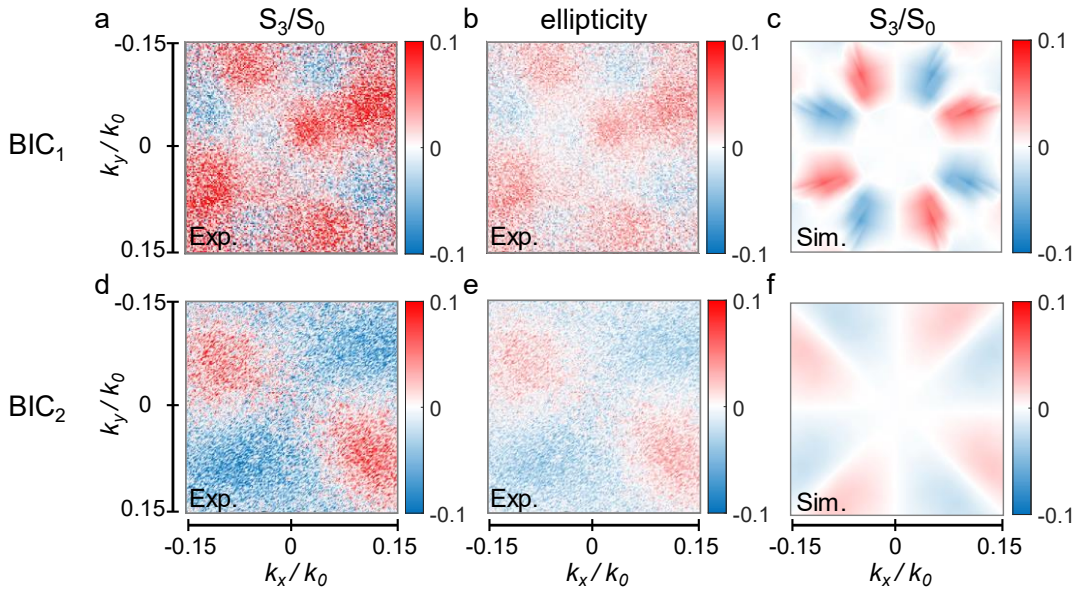

Figure S11 Stokes parameter S_3/S_0 and ellipticity of PL in *k*-space for Circular polarization emission. The measured (a) and simulated (c) of BIC_1 bands correspond to the Stokes parameters S_3/S_0 representing the circular polarization characteristics, and the BIC_2 bands correspond to panels (d) and (f), respectively. Panels (b)(e) show the ellipticity angles χ calculated from panels (a) and (d).

S7 Comparison of directional emission enhancement characteristics with the reported results from literature

Table S1 provides a summary of representative research efforts in the past decade focused on enhancing out-coupling efficiency of the extended emitting layer. The table includes studies involving Ag and Al nanoparticle arrays that support plasmonic resonances, as well as dielectric nanostructures exhibiting Mie resonances (e.g., Si, TiO_2, and GaN). Note that the results presented in this work are in bold. Previous reports (Ref.17-20) have demonstrated PL enhancements of up to ~10^3, but these enhancements are not solely attributed to directional emission provided by the structures. Specifically, the directional emission enhancements achieved in Refs. 10, 12, and 16 are only around 10-fold. In contrast, our work has achieved a directional emission enhancement that is increased up to four times through the control of multipole resonances and lattice periodicities. The maximum directionality enhancement attained in our study is approximately 41-fold, thereby advancing the development of efficient micro and nanoscale light sources as well as low-threshold lasers.

Table S1 A comparison of the PL enhancement characteristics with literatures

Structures	Resonances	Integrate emitters with structure	Emitting layers	Emission wavelength	Directional emission enhancement (PLE)	Reference
c-Si nanoparticle arrays (NPAs)	**Quasi-BICs**	**Covering the NPAs with emitters**	**300 nm dye film**	**675 nm**	**41-fold (92-fold)**	**This work**
Quartz hole arrays	Quasi-BICs	Fill the holes with emitters	30 nm perovskite films	539 nm	(17-fold)	9
Al nanoparticle arrays	Plasmonic SLRs and quasi-guided modes (QGMs)	Covering the NPAs with emitters	650 nm dye film	608 nm	10-fold (60-fold)	10
Al nanoparticle arrays	Plasmonic SLRs and QGMs	Covering the NPAs with emitters	700 nm dye film	638 nm	(14-fold)	11
Poly-Si nanoparticle arrays	Mie SLRs	Covering the NPAs with emitters	300 nm dye film	640 nm	10-fold	12
a-Si nanoparticle arrays	Mie resonances	Covering the NPAs with emitters	3 nm quantum dots	790 nm	(1.45-fold)	13
Polymer nanoparticle arrays on DBR mirror	Mie resonances	Covering the NPAs with emitters	~ 10 nm perovskite nanocrystals	650 nm	(16-fold)	14
Si nanoparticle arrays	Mie SLRs	Placing the NPAs on glass substrate	defects of glass	850 nm	4-fold (28-fold)	15
TiO_2 nanoparticle arrays	Rayleigh anomaly	Placing the NPAs on phosphor substrate	105 μm phosphor substrate	520 nm	12-fold	16
GaN nanowire array	Hybrid of Guiding modes and Mie resonances	Embedding the emitters inside the nanowires	3 nm InGaN Quantum wells	540 nm	(100-fold)	17
a-Si nanogap arrays	Mie resonances	Filling the monolayer in the nanogap	Monolayer molecules	530 nm	2.45-fold (1200-fold)	18
a-Si hole array	Mie resonances	Embedding the emitters inside the metasurface	8 nm Ge quantum dots	1507 nm	(1097-fold)	19
a-Si nanoparticle arrays	Quasi-BICs	Embedding the emitters inside the metasurface	30 nm Er-doped silica	1540 nm	(100-1000 fold)	20
Disordered Ag nanoparticles	Plasmonic resonances	Placing the particles on emitting layer	Commercial blue LED	450 nm	(~1.7-fold)	21
Ag nanoparticle arrays	Plasmonic SLRs and Fabry-Perot cavity	Placing the emitting layer on top of the planarized NPAs	Commercial OLED	450 nm, 530 nm, 630 nm	(~ 2-fold)	22

Supplementary References

[1] Zhang, Z.; Liu, P.; Lu, W.; Bai, P.; Zhang, B.; Chen, Z.; Maier, S. A.; Rivas, J. G.; Wang, S.; Li, X. High-Q collective Mie resonances in monocrystalline silicon nanoantenna arrays for the visible light. *Fundamental Research* **2022**, doi.org/10.1016/j.fmre.2022.05.020.

[2] Uno, K.; Niikura, H.; Morimoto, M.; Ishibashi, Y.; Miyasaka, H.; Irie, M. In situ preparation of highly fluorescent dyes upon photoirradiation. Journal of the American Chemical Society **2011**, 133, 13558–13564.

[3] Vaskin, A.; Kolkowski, R.; Koenderink, A. F.; Staude, I. Light-emitting metasurfaces. Nanophotonics **2019**, 8, 1151–1198.

[4] Lieb, M. A.; Zavislan, J. M.; Novotny, L. Single-molecule orientations determined by direct emission pattern imaging. Journal of the Optical Society of America B **2004**, 21, 1210–1215.

[5] Berry, H. G.; Gabrielse, G.; Livingston, A. Measurement of the Stokes parameters of light. Applied Optics **1977**, 16, 3200–3205.

[6] Ramezani, M.; Lozano, G.; Verschuuren, M. A.; Gómez-Rivas, J. Modified emission of extended light emitting layers by selective coupling to collective lattice resonances. Physical Review B **2016**, 94, 125406.

[7] Novotny, L.; Hecht, B. Principles of Nano-optics; Cambridge university press, **2012**.

[8] Zhen, B.; Hsu, C. W.; Lu, L.; Stone, A. D.; Soljačić, M. Topological nature of optical bound states in the continuum. Physical Review Letters **2014**, 113, 257401.

[9] Kim, S.; Woo, B. H.; An, S.-C.; Lim, Y.; Seo, I. C.; Kim, D.-S.; Yoo, S.; Park, Q.-H.; Jun, Y. C. Topological control of 2D perovskite emission in the strong coupling regime. *Nano Letters* **2021**, 21, 10076–1008.

[10] Lozano, G.; Louwers, D. J.; Rodríguez, S. R.; Murai, S.; Jansen, O. T.; Verschuuren, M. A.; Gómez Rivas, J. Plasmonics for solid-state lighting: enhanced excitation and directional emission of highly efficient light sources. *Light: Science & Applications* **2013**, 2, e66–e66.

[11] Wang, S.; Le-Van, Q.; Peyronel, T.; Ramezani, M.; Van Hoof, N.; Tiecke, T. G.; Gomez Rivas, J. Plasmonic nanoantenna arrays as efficient etendue reducers for optical detection. *ACS Photonics* **2018**, 5, 2478–2485.

[12] Murai, S.; Castellanos, G. W.; Raziman, T.; Curto, A. G.; Rivas, J. G. Enhanced light emission by magnetic and electric resonances in dielectric metasurfaces. *Advanced Optical Materials* **2020**, 8, 1902024.

[13] Hasebe, H.; Sugimoto, H.; Hinamoto, T.; Fujii, M. Coupled toroidal dipole modes in silicon nanodisk metasurface: polarization independent narrow band absorption and directional emission. *Advanced Optical Materials* **2020**, 8, 2001148.

[14] Carreño, J. M.; Passarelli, N.; Otero-Martínez, C.; Polavarapu, L.; Pérez, L. A.; Reparaz, J. S.; Alonso, M. I.; Mihi, A. Enhanced Photoluminescence of Cesium Lead Halide Perovskites by Quasi-3D Photonic Crystals. *Advanced Optical Materials* **2022**, 10, 2101324.

[15] Vaskin, A.; Bohn, J.; Chong, K. E.; Bucher, T.; Zilk, M.; Choi, D.-Y.; Neshev, D. N.; Kivshar, Y. S.; Pertsch, T.; Staude, I. Directional and spectral shaping of light emission with Mie-resonant silicon nanoantenna arrays. *ACS Photonic*s **2018**, 5, 1359–1364.

[16] Murai S.; Zhang F.; Aichi K.; Tanaka K. Photoluminescence engineering with nanoantenna phosphors, *Journal of Materials Chemistry C* **2023**, 11, 472-479.

[17] Iyer P.; DeCrescent RA; Mohtashami Y; Lheureux G, Butakov NA, Alhassan A, Weisbuch C, Nakamura S, DenBaars SP, Schuller JA. Unidirectional luminescence from InGaN/GaN quantum-well metasurfaces. *Nature Photonics* **2020**, 9, 543-548.

[18] Dong, Z.; Gorelik, S.; Paniagua-Dominguez, R.; Yik, J.; Ho, J.; Tjiptoharsono, F.; Lassalle, E.; Rezaei, S. D.; Neo, D. C.; Bai, P., et al. Silicon nanoantenna mix arrays for atrifecta of quantum emitter enhancements. *Nano Letters* **2021**, 21, 4853–4860.

[19] Yuan, S.; Qiu, X.; Cui, C.; Zhu, L.; Wang, Y.; Li, Y.; Song, J.; Huang, Q.; Xia, J. Strong photoluminescence enhancement in all-dielectric Fano metasurface with high quality factor. *ACS Nano* **2017**, 11, 10704-10711.

[20] Kalinic, B.; Cesca, T.; Balasa, I. G.; Trevisani, M.; Jacassi, A.; Maier, S. A.; Sapienza, R.; Mattei, G. Quasi-BIC Modes in All-Dielectric Slotted Nanoantennas for Enhanced Er3+ Emission. *ACS Photonics* **2023**, doi.org/10.1021/acsphotonics.2c01703.

[21] Mao, P.; Liu, C.; Li, X.; Liu, M.; Chen, Q.; Han, M.; Maier, S. A.; Sargent, E. H.; Zhang, S. Single-step-fabricated disordered metasurfaces for enhanced light extraction from LEDs. *Light: Science & Applications* **2021**, 10, 180.

[22] Joo, W.-J.; Kyoung, J.; Esfandyarpour, M.; Lee, S.-H.; Koo, H.; Song, S.; Kwon, Y.-N.; Song, S. H.; Bae, J. C.; Jo, A., et al. Metasurface-driven OLED displays beyond 10,000 pixels per inch. *Science* **2020**, 370, 459–463.